Coherent x-ray wavefront reconstruction of a partially illuminated Fresnel zone plate

F. Mastropietro,[1,2,*] D. Carbone,[2] A. Diaz,[2,5] J. Eymery,[1] A. Sentenac,[3] T. H. Metzger,[2,6] V. Chamard,[3] and V. Favre-Nicolin[1,4]

[1]*SP2M / UMR-E CEA / UJF-Grenoble 1, INAC, Grenoble, F-38054, France*
[2]*European Synchrotron Radiation Facility, BP220, 38043 Grenoble, France*
[3]*Institut Fresnel, CNRS, Aix-Marseille Université, Ecole Centrale Marseille, Campus de St. Jérôme, 13013 Marseille, France*
[4]*Université Joseph Fourier, Grenoble, France*
[5]*Current address: Paul Sherrer Institut, Swiss Light Source, WLGA-225, Switzerland*
[6]*Current address: Max Planck Institute of Colloids and Interfaces, Department of Biomaterials, 14424 Potsdam, Germany*
[*]*francesca.mastropietro@esrf.fr*

Abstract: A detailed characterization of the coherent x-ray wavefront produced by a partially illuminated Fresnel zone plate is presented. We show, by numerical and experimental approaches, how the beam size and the focal depth are strongly influenced by the illumination conditions, while the phase of the focal spot remains constant. These results confirm that the partial illumination can be used for coherent diffraction experiments. Finally, we demonstrate the possibility of reconstructing the complex-valued illumination function by simple measurement of the far field intensity in the specific case of partial illumination.

OCIS codes: (340.0340) X-ray optics; (340.7440) X-ray imaging.

References and links

1. K. A. Nugent, "Coherent methods in the x-ray sciences," Adv. Phys. **59**, 1–99 (2010).
2. V. L. R. Jacques, S. Ravy, D. L. Bolloc'h, E. Pinsolle, M. Sauvage-Simkin, and F. Livet, "Bulk dislocation core dissociation probed by coherent x rays in silicon," Phys. Rev. Lett. **106**, 065502 (2011).
3. V. Chamard, J. Stangl, S. Labat, B. Mandl, R. T. Lechner, and T. H. Metzger, "Evidence of stacking-fault distribution along an InAs nanowire using micro-focused coherent x-ray diffraction," J. Appl. Cryst. **41**, 272–280 (2008).
4. J. Miao, P. Charalambous, J. Kirz, and D. Sayre, "Extending the methodology of x-ray crystallography to allow imaging of micrometre-sized non-crystalline specimens," Nature **400**, 342–344 (1999).
5. M. Dierolf, A. Menzel, P. Thibault, P. Schneider, C. M. Kewish, R. Wepf, O. Bunk, and F. Pfeiffer, "Ptychographic x-ray computed tomography at the nanoscale," Nature **467**, 436–439 (2010).
6. S. Eisebitt, J. Lüning, W. F. Schlotter, M. Lorgen, O. Hellwig, W. Eberhardt, and J. Stohr, "Lensless imaging of magnetic nanostructures by x-ray spectro-holography," Nature **432**, 885–888 (2004).
7. F. Pfeiffer, T. Weitkamp, O. Bunk, and C. David, "Phase retrieval and differential phase-contrast imaging with low-brilliance x-ray sources," Nat. Phys. **2**, 258–261 (2006).
8. V. Favre-Nicolin, J. Eymery, R. Koester, and P. Gentile, "Coherent-diffraction imaging of single nanowires of diameter 95 nanometers," Phys. Rev. B **79**, 195401 (2009).
9. M. C. Newton, S. J. Leake, R. Harder, and I. K. Robinson, "Three-dimensional imaging of strain in a single ZnO nanorod," Nat. Mater. **9**, 120–124 (2010).
10. P. Godard, D. Carbone, M. Allain, F. Mastropietro, G. Chen, A. Diaz, T. H. Metzger, J. Stangl, and V. Chamard, "Three-dimensional x-ray Bragg ptychography: high-resolution imaging of extended crystalline nanostructures," Submitted to Nat. Commun.

#146854 - $15.00 USD Received 5 May 2011; revised 3 Jun 2011; accepted 3 Jun 2011; published 19 Sep 2011

11. V. Chamard, J. Stangl, G. Carbone, A. Diaz, G. Chen, C. Alfonso, C. Mocuta, and T. H. Metzger, "Three-dimensional x-Ray Fourier transform holography: the Bragg case," Phys. Rev. Lett. **104**, 165501 (2010).
12. R. W. Gerchberg and W. O. Saxton, "A practical algorithm for the determination of the phase from image and diffraction plane pictures," Optik **35**, 237–246 (1972).
13. J. R. Fienup, "Phase retrieval algorithms: a comparison," Appl. Opt. **21**, 2758–2769 (1982).
14. S. Marchesini, H. He, H. N. Chapman, S. P. Hau-Riege, A. Noy, M. R. Howells, U. Weierstall, and J. C. H. Spence, "X-ray image reconstruction from a diffraction pattern alone," Phys. Rev. B **68**, 140101 (2003).
15. S. Takagi, "A dynamical theory of diffraction for a distorted crystal," J. Phys. Soc. Jpn. **26**, 1239–1253 (1969).
16. A. Snigirev, V. Kohn, I. Snigireva, A. Souvorov, and B. Lengeler, "Focusing high-energy x-rays by compound refractive lenses," Appl. Opt. **37**, 653–662 (1998).
17. K. Yamauchi, H. M. Mimura, K. Yamamura, Y. Sano, H. Yumoto, S. Matsuyama, K. Endo, Y. Nishino, K. Tamasaku, M. Yabashi, T. Ishikawa, and Y. Mori "Development of elliptical Kirkpatrick-Baez mirrors for hard x-ray nanofocusing," *Frontiers in Optics*, OSA Technical Digest Series (Optical Society of America, 2005), paper FTuS4.
18. D. M. Paganin, *Coherent X-ray Optics*, Oxford series on synchrotron radiation (Oxford University Press, 2006), Vol. 6.
19. W. Chao, B. D. Harteneck, J. A. Liddle, E. H. Anderson, and D. T. Attwood, "Soft x-ray microscopy at a spatial resolution better than 15nm," Nature **435**, 1210–1213 (2005).
20. E. D. Fabrizio, F. Romanato, M. Gentili, S. Cabrini, B. Kaulich, J. Susini, and R. Barrett, "High-efficiency multilevel zone plates for keV x-rays," Nature **401**, 895–898 (1999).
21. C. G. Schroer, P. Boye, J. M. Feldkamp, J. Patommel, A. Schropp, A. Schwab, S. Stephan, M. Burghammer, S. Schöder, and C. Riekel, "Coherent x-ray diffraction imaging with nanofocused illumination," Phys. Rev. Lett. **101**, 090801 (2008).
22. I. A. Vartanyants and I. K. Robinson, "Partial coherence effects on the imaging of small crystals using coherent x-ray diffraction," J. Phys. Condens. Matter **13**, 10593–10611 (2001).
23. A. Diaz, C. Mocuta, J. Stangl, B. Mandl, C. David, J. Vila-Comamala, V. Chamard, T. H. Metzger, and G. Bauer, "Coherent diffraction imaging of a single epitaxial InAs nanowire using a focused x-ray beam," Phys. Rev. B **79**, 125324 (2009).
24. Http://www.esrf.eu/UserAndScience/Experiments/StructMaterials/ID01.
25. G. J. Williams, H. M. Quiney, B. B. Dhal, C. Q. Tran, K. A. Nugent, A. G. Peele, D. Paterson, and M. D. de Jonge, "Fresnel coherent diffractive imaging," Phys. Rev. Lett. **97**, 025506 (2006).
26. K. A. Nugent, A. G. Peele, H. M. Quiney, and H. N. Chapman, "Diffraction with wavefront curvature: a path to unique phase recovery," Acta Cryst. A **61**, 373–381 (2005).
27. V. Chamard, A. Diaz, J. Stangl, and S. Labat, "Structural investigation of InAs nanowires with coherent x-rays," J. Strain Anal. Eng. Des. **44**, 533–542 (2009).
28. P. Thibault, M. Dierolf, A. Menzel, O. Bunk, C. David, and F. Pfeiffer, "High-resolution scanning x-ray diffraction microscopy," Science **321**, 379–382 (2008).
29. C. M. Kewish, P. Thibault, M. Dierolf, O. Bunk, A. Menzel, J. Vila-Comamala, K. Jefimovs, and F. Pfeiffer, "Ptychographic characterization of the wavefield in the focus of reflective hard x-ray optics," Ultramicroscopy **110**, 325–329 (2010).
30. H. M. Quiney, A. G. Peele, Z. Cai, D. Paterson, and K. A. Nugent, "Diffractive imaging of highly focused x-ray fields," Nat. Phys. **2**, 101–104 (2006).
31. A. Diaz, C. Mocuta, J. Stangl, M. Keplinger, T. Weitkamp, F. Pfeiffer, C. David, T. H. Metzger, and G. Bauer, "Coherence and wavefront characterization of Si-111 monochromators using double-grating interferometry," J. Synchrotron Radiat. **17**, 299–307 (2010).
32. S. Gorelick, J. Vila-Comamala, V. A. Guzenko, R. Barrett, M. Salomé, and C. David, "High-efficiency Fresnel zone plates for hard x-rays by 100keV e-beam lithography and electroplating," J. Synchrotron Radiat. **18**, 442–446 (2011).
33. C. David, B. Nöhammer, E. Ziegler, and O. Hignette, "Tunable diffractive optical elements for hard x-rays," Proc. SPIE **4499**, 96–104 (2001).
34. C. Ponchut, J. M. Rigal, J. Clément, E. Papillon, A. Homs, and S. Petitdemange, "Maxipix, a fast readout photon-counting x-ray area detector for synchrotron applications," J. Instrum. **6**, C01069 (2011).
35. J. Vila-Comamala, S. Gorelick, E. Färm, C. M. Kewish, A. Diaz, R. Barrett, V. A. Guzenko, M. Ritala, and C. David, "Ultra-high resolution zone-doubled diffractive x-ray optics for the multi-kev regime," Opt. Express **19**, 175–184 (2011).
36. O. Bunk, A. Diaz, F. Pfeiffer, C. David, B. Schmitt, D. K. Satapathy, and J. F. van der Veen, "Diffractive imaging for periodic samples: retrieving one-dimensional concentration profiles across microfluidic channels," Acta Cryst. A **63**, 306–314 (2007).
37. D. L. Bolloc'h, F. Livet, F. Bley, T. Schülli, M. Veron, and T. H. Metzger, "X-ray diffraction from rectangular slits," J. Synchrotron Radiat. **9**, 258–265 (2002).

#146854 - $15.00 USD Received 5 May 2011; revised 3 Jun 2011; accepted 3 Jun 2011; published 19 Sep 2011

1. Introduction

Diffraction of coherent x-ray beams such as the ones delivered by third generation synchrotron sources [1] is a powerful tool to probe structural properties in condensed matter. The well-defined phase relation of the coherent wavefront, which is preserved through the scattering process, assures a high sensitivity to the exact position of the single scatterers [2, 3]. This is the basic principle of lens-less microscopy techniques as coherent diffraction imaging (CDI), Fourier transform holography and ptychography, aiming at the model-free investigation of materials at the sub-micron scale. These techniques are based on the measurement of far-field coherent intensity patterns; from those, numerical methods are used to retrieve at the sample position the complex exit wavefield $E(\mathbf{r})$, where $\mathbf{r}$ defines the scatterer position inside the sample. Due to the weak interaction of x-rays with matter, the Born approximation can be used to relate the exit wavefield $E(\mathbf{r})$ to the product of the complex-valued function $\rho(\mathbf{r})$, that describes the sample, and the illumination probe $\psi(\mathbf{r})$. As long as we can assume that the focal spot of $\psi(\mathbf{r})$ has a constant phase, the exit wavefield $E(\mathbf{r})$ coincides with the sample scattering function $\rho(\mathbf{r})$. The cited lens-less microscopy approaches have been largely applied in the forward direction, i.e. small angle scattering regime [4–6]. In this case $\rho(\mathbf{r})$ is interpreted as the electron density of the object and morphological information like shape and density are obtained. The use of coherent diffraction techniques in Bragg geometry [7–11] gives access to the strain fields encoded in the phase of the complex function $\rho(\mathbf{r})$. In the case of CDI and ptychography, the phase is reconstructed by means of iterative phase retrieval algorithms [12–14], while in holography it is directly measured with the intensity interference pattern. In all cases, the retrieved phase represents in good approximation the projection of the displacement of the crystalline lattice onto the scattering vector [15].

The recent development of dedicated focusing optics, i.e. compound refractive lenses (CRL) [16], Kirckpatrick-Baez (KB) mirrors [17] and Fresnel Zone Plate (FZP) [18–20] offers the possibility of focusing x-ray beams to sub-micron size to increase the photon flux while preserving the wavefront of the coherent beam [21]. This allows the exploitation of lens-less microscopy methods for the investigation of matter at the nanoscale. However, x-rays provided by a third generation synchrotron source have only partial coherence properties [22], with typical transverse coherence lengths in the 10-100 μm range for hard x-rays. A lens with a radius small enough to match these lengths can be used to ensure the coherent illumination at the expense of reducing the focal distance, which decreases linearly with the lens diameter. Hence, a good compromise between the preservation of working distances and the loss of photon flux can be obtained reducing the illuminated area on the lens by means of an opening (partial illumination) matching the coherent lengths [23] . This approach, which is at the focus of the present manuscript, is particularly interesting for short synchrotron beamlines, e.g. the undulator beamline ID01 at the European Synchrotron Radiation Facility (ESRF, Grenoble) [24] distant 50 m from the source. The partial illumination necessarily affects the wavefront of the focused x-ray beam with a consequent modification of the exit wavefield. Consequently, the strong contribution of $\psi(\mathbf{r})$ in the retrieved exit field $E(\mathbf{r})$ has to be ruled out, as a local wavefront curvature or a change in the phase of the illuminating complex field affect the sample reconstruction [25–27]. Therefore, an accurate investigation of the sample requires a detailed knowledge of the probe wavefront. Unfortunately, the resolution of available 2D detectors does not allow to perform direct imaging of the focal spot. A solution to this problem is offered by the ptychography approach, that enables the simultaneous reconstruction of the sample electron density and the illumination function [28, 29]. However, the convergence of the inversion process relies on a reasonable a priori knowledge of the initial probe estimate in terms of typical width and shape. In the case of weak scattering objects, a good knowledge of the initial probe is mandatory [5].

#146854 - $15.00 USD Received 5 May 2011; revised 3 Jun 2011; accepted 3 Jun 2011; published 19 Sep 2011

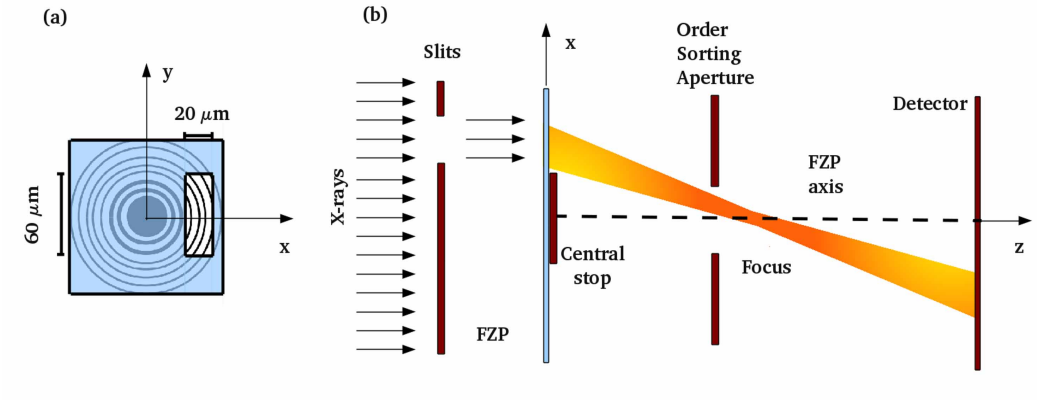

Fig. 1. (a) Sketch of a partially illuminated Fresnel Zone Plate. A pair of slits defines a rectangular aperture matching the transverse coherence lengths of the x-ray beam. (b) 2D schematic of the propagation of the wavefield produced by a partially illuminated FZP. The slits, placed 1.15 m upstream the lens, used to define the illuminated area, the FZP, the CS and the OSA are represented. The effective direction of propagation is tilted with respect to the FZP axis due to the lateral displacement of the slits.

In this work, based on numerical and experimental approaches, we propose a detailed characterization of the wavefront produced by a partially illuminated circular FZP with the aim of disentangling the contributions of $\psi(\mathbf{r})$ and $\rho(\mathbf{r})$ to the retrieved exit field $E(\mathbf{r})$. Our simulations allow to predict and understand the influence of the partial illumination of a FZP demonstrating that this approach can be used to produce a focal spot with a constant phase. Finally we show the possibility of reconstructing the amplitude and phase of the wavefront of the illumination function by simple measurement of the intensity in the divergent part of the focused beam as proposed in Ref. [30] also in the specific case of partial illumination conditions. The manuscript is organized as follows: in section 2, the experimental set-up is described together with the associated numerical tools to simulate, fit and retrieve the wavefront at the focus. Section 3 illustrates the numerical results obtained for different partial illumination conditions, which are further used to fit the experimental data. The last section discusses the possibility to reconstruct the wavefront directly from experimental intensity pattern at the detector.

2. Experimental set-up and numerical tools

2.1. The nano-focusing set-up for coherent diffraction at ID01

This work is based on the set-up used on the ID01 beamline at the ESRF for coherent diffraction experiments. This undulator beamline has an effective source size, measured after the monochromator, of $125_h \times 30_v$ μm^2 (FWHM) in the horizontal (h) and vertical (v) directions, respectively [31]. At the sample position, 50 m downstream from the source, the transverse coherence lengths are $60_v \times 20_h$ μm^2 (FWHM).

Figure 1 shows the schematics of the set-up. A 200 μm diameter gold FZP with an outermost zone width of 70 nm [32] is used to focus the coherent beam. The thickness of the zones is equal to 1 μm. This provides an efficiency of 15% in the 6 - 9 keV energy range [33]. At 8 keV, the energy used during the experiments, the calculated focal length is $L = 0.09$ m. As the FZP diameter is larger than the coherence lengths, a pair of slits located 1.15 m upstream the FZP is used to provide the partial illumination. The slit aperture is laterally shifted (Fig. 1a)

#146854 - $15.00 USD Received 5 May 2011; revised 3 Jun 2011; accepted 3 Jun 2011; published 19 Sep 2011

to avoid the illumination of the central stop (CS). A 65 μm diameter CS and an order sorting aperture (OSA) with a diameter of 50 μm are introduced to avoid direct beam contribution and to block higher diffraction orders (Fig. 1b). The measurements of the direct beam in the forward direction are performed in the far-field regime using a Maxipix 2D pixel detector, with 256×256 pixels of 55×55 μm^2 size [34]. This photon counting detector produces zero read-out noise and is installed at a distance of 0.954 m downstream the focal plane (Fig. 1b, not in scale).

2.2. *Wavefront propagation: numerical calculations*

The models used for the propagation of the wavefront produced by a partially illuminated FZP are detailed in this section. For all the numerical simulations, we assume a monochromatic and fully coherent beam. In the (x,y,z) laboratory frame, x (horizontal direction) and y (vertical direction) define the plane perpendicular to the direction of propagation z, i.e. FZP axis (Fig. 1). In the partial illumination conditions, due to the absence of an axial symmetry, the propagation is computed using a three-dimensional complex field $\Psi(x,y,z)$. This makes simulations more computationally demanding with respect to the case of full illumination condition [35]. The origin of the reference frame is set at the FZP position. The initial wavefield $\Psi(x,y,z_{FZP})$, where $z_{FZP} = 0$, is defined as:

$$\Psi(x,y,z_{FZP}) \propto \exp\big(-i\phi_{FZP} f_{FZP}(r_n)\big) \times M_1(x,y) \tag{1}$$

where $f_{FZP}(r_n)$ is function of the radius $r_n \simeq \sqrt{n\lambda f}$ for $n = 1, ..., number\ of\ zones$, and represents the zone plate profile and λ is the wavelength. The phase factor ϕ_{FZP} defines the phase shift occurring when x-ray propagate through the zones and depends on the structural characteristics of the FZP. $M_1(x,y)$ is a mask function that takes into account the presence of both CS and rectangular slits. For the first calculations, we neglected the propagation of the beam from the slits to the FZP. However, we know that, for a satisfactory comparison with data, such a propagation must be taken into account.

The propagation of the exit field $\Psi(x,y,z_{FZP})$ along z is performed through [36] :

$$\Psi(x,y,z) = FT^{-1}\Big(P_z(\mathbf{q},z) FT\big(\Psi(x,y,z_{FZP})\big)\Big), \tag{2}$$

where FT denotes the Fourier Transform operator and $P_z(\mathbf{q},z) = \exp(-iz\ q^2/2k)$ is the Fresnel propagator in Fourier space. At $z = z_{OSA}$ the propagated field $\Psi(x,y,z_{OSA})$ is multiplied with a mask $M_2(x,y)$, modelling the OSA. The resulting field is further propagated to the focal plane. For the numerical calculations, the two dimensional zone plate has been computed using a pixel size of 20 nm, as a compromise between the available computer memory and the resolution required to define the outermost zone width. At 8 keV, the FZP phase shift is 1.39 rad. The OSA is introduced at $z_{OSA} = 0.08$ m.

The final step of our calculations is the wavefront propagation to the detector position according to the paraxial Fresnel free-space approximation. This approach, equivalent to Eq. (2), operates in *direct* rather than *reciprocal* space [30] using the following formula:

$$\begin{aligned} \Psi(x_f,y_f,z_f) \quad = \quad & -\frac{i}{\lambda z_{if}} \exp\left(\frac{2\pi i z_{if}}{\lambda}\right) \exp\left(\frac{\pi i {\rho_\mathbf{i}}^2}{\lambda z_{if}}\right) \\ & \times \int\int \Psi(x_i,y_i,z_i) \exp\left(\frac{\pi i {\rho_\mathbf{i}}^2}{\lambda z_{ij}}\right) \exp\left(-\frac{2\pi i \rho_\mathbf{i} \cdot \rho_\mathbf{f}}{\lambda z_{if}}\right) dx_i\, dy_i, \end{aligned} \tag{3}$$

where $z_{if} = z_i - z_f$ is the distance between the initial (i) and the final (f) positions along the propagation axis, $\rho^2 = x^2 + y^2$ defines the radial distance from the optical axis in the xy plane.

#146854 - $15.00 USD Received 5 May 2011; revised 3 Jun 2011; accepted 3 Jun 2011; published 19 Sep 2011

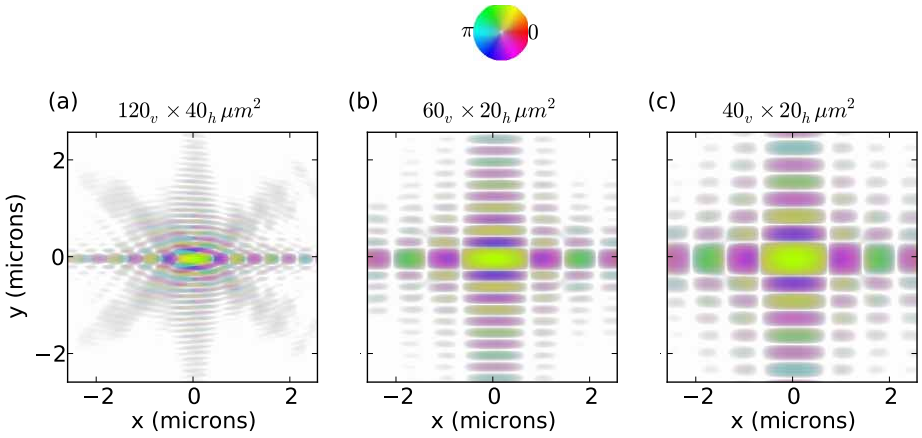

Fig. 2. Simulated complex field at the focal plane of a Fresnel Zone Plate for different conditions of partial illumination. Color rendition of the complex-valued probe for (a) $120_v \times 40_h$, (b) $60_v \times 20_h$ and (c) $40_v \times 20_h$ μm^2 slits aperture. The phase is represented by colors and the amplitude (in logarithmic scale) by colors intensities.

This choice allows to handle smaller two-dimensional matrices, reducing both computational memory and time, and to rescale the pixel size of the matrices at each position along the propagation. For our numerical simulations, a range $\Delta x \approx 2.6$ μm, corresponding to 129 pixels of 20 nm, has been selected at the focal plane to obtain a pixel size d_{pxl} of 57 μm at the detector plane, calculated through the formula: $d_{pxl} \approx \frac{\lambda}{2N\Delta\theta}$, where $\Delta\theta = \arcsin(\lambda\ \Delta x)$ is the angular resolution at the detector plane and N the total number of pixels.

2.3. Phase retrieval algorithm

In order to reconstruct the wavefront at the focal plane we use the phase retrieval algorithm described in Ref. [30]. In this algorithm the Fourier transform approach is replaced in both directions (from lens to detector and vice versa) by Eq. (3). According to the proposed method, the wavefront reconstruction is done without employing any sample at the focal position. The wavefield at the focus is retrieved from the direct beam intensity at the detector position. The algorithm, consisting of error reduction , hybrid input-output and charge flipping cycles, can be summarized in three steps and follows the cycle: detector-focus-FZP. To make the algorithm converging, constraints are applied both in direct and reciprocal space. The support, whose size is defined by the illuminated area on the lens, is added at the FZP position with the shrink-wrap algorithm [14] and the calculated intensity at the detector is replaced by experimental data. At each iteration, the reconstruction is controlled using the metric error.

3. Wavefront of a partially illuminated FZP : numerical calculations

In this section we discuss the effects of the partial illumination of the FZP on the focused beam characteristics. The results shown are fully based on simulation described in section 2.2. The theoretical values obtained in the case a fully illuminated FZP are used as comparison. In this case, the focal depth and the focal spot size are 290 μm and $85_v \times 85_h$ nm^2, respectively, and the phase of the focal spot is constant. Figure 2 shows the calculations in the case of partial

#146854 - $15.00 USD Received 5 May 2011; revised 3 Jun 2011; accepted 3 Jun 2011; published 19 Sep 2011

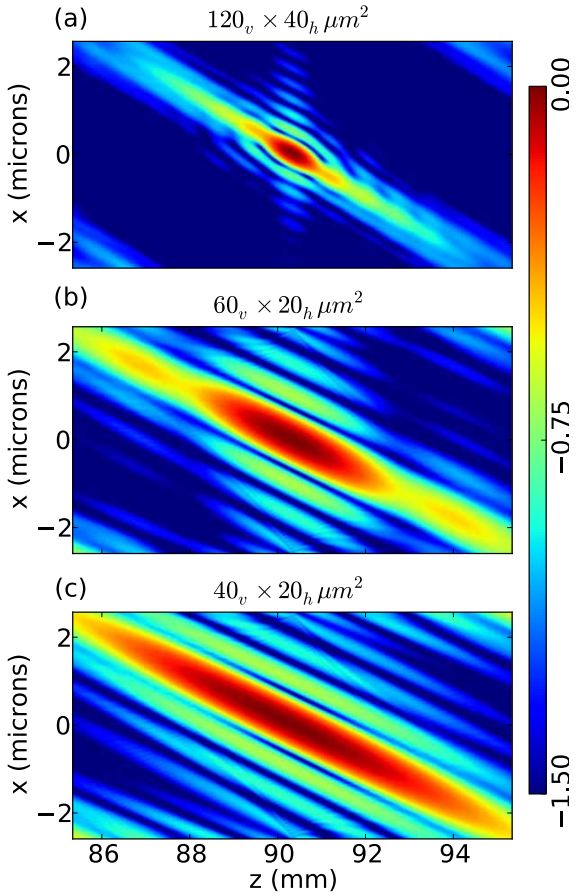

Fig. 3. Section of the simulated complex field in the direction of propagation for different conditions of partial illumination. Amplitude (expressed in logarithmic scale) for an opening of (a) $120_v \times 40_h$, (b) $60_v \times 20_h$ and (c) $40_v \times 20_h$ μm^2.

Table 1. Values of Beam Size and Focal Depth Calculated for Different Illumination Conditions*

Slit Opening μm^2	Focal Spot Size (FWHM) μm^2	Focal depth (FWHM) mm	Phase rad
$200_v \times 200_h$	$0.085_v \times 0.085_h$	0.29	const.
$120_v \times 40_h$	$0.20_v \times 0.58_h$	0.74	const.
$60_v \times 20_h$	$0.39_v \times 1.20_h$	2.66	const.
$40_v \times 20_h$	$0.60_v \times 1.20_h$	5.68	const.

*Calculated phases at the focal spot is also tabulated. The ideal case of a fully illuminated FZP is shown for comparison.

#146854 - $15.00 USD Received 5 May 2011; revised 3 Jun 2011; accepted 3 Jun 2011; published 19 Sep 2011

illumination. In order to simulate our experimental conditions, a slit opening of $60_v \times 20_h$ μm^2 has been chosen to match the transverse coherent length of the x-ray beam used. Two additional illumination conditions have been used for comparison: $120_v \times 40_h$ μm^2 - which corresponds to the transverse coherence at a double distance from the source. This choice is motivated by the planned upgrade programme for the extended ID01 beamline. A $40_v \times 20_h$ μm^2 slit aperture has been also used, as a lower size limit. Both focal depth and transverse dimensions of the focal spot are strongly influenced by the opening. The beam size is diffraction limited: the wavefront profile is related to the slit opening and to the number of illuminated zones. The focal spot becomes larger for smaller openings (Figs. 2a-2c). The focal depth is also inversely proportional to the slit opening (Fig. 3) and it is found to be significantly larger than the one observed in the case of a fully illuminated FZP. This effect is attributed to the decreased numerical aperture of the lens, i.e. the smaller divergence of the beam produced with a slit smaller than the transverse FZP dimensions. One can see that the effective direction of propagation is tilted with respect to the Fresnel Zone Plate axis by 0.47 mrad (Fig. 3). This is due to the lateral shift of the illuminated area on the lens (cf. Fig. 1). This shift produces a linear phase in the focal plane which has been corrected in Figs. 2a-2c. The corrected phases refer to a plane wave along the effective direction of propagation. This allows to emphasize the constant phase near the center of the focal spot. These results indicate that the partial illumination of the FZP does not affect the phase of the focused beam, which justifies the plane wave assumption in CDI experiments, as long as the object studied is smaller than the focal spot. The values of the simulated focal spot dimensions are summarized in Table 1 together with the full illumination case to emphasize the influence of slits.

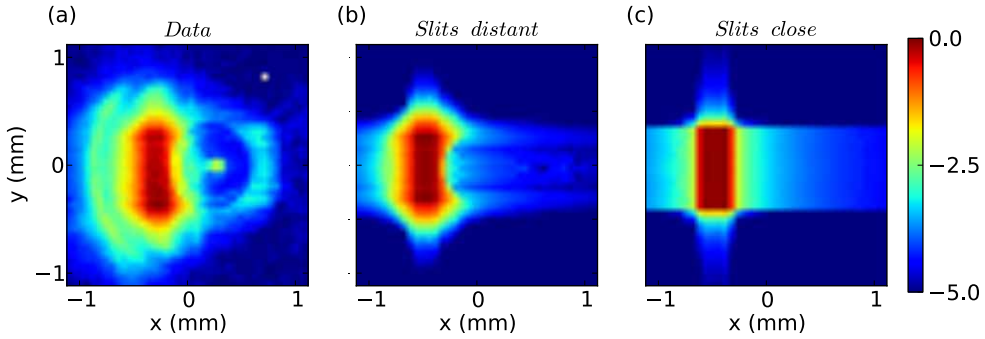

Fig. 4. (a) Measured intensities in logarithmic scale of the illumination probe at the detector. It is compared to (b) simulated intensities with the slits distant 1.15 *m* from the lens plane and (c) close (neglecting the propagation from the slits) to the FZP. The best agreement is obtained with a slit opening of $72_v \times 28_h$ μm^2. The non-zero intensity pixels in the center of the detector are due to direct beam photons transmitted by the central stop.

4. Propagation to the detector plane and comparison with measurements

A typical measurement of the direct beam at the detector position is shown in Fig. 4a. Using the numerical tools described in section 2, the x-ray propagation to the detector plane can be

#146854 - $15.00 USD Received 5 May 2011; revised 3 Jun 2011; accepted 3 Jun 2011; published 19 Sep 2011

simulated using different slits opening until an agreement with experimental data is found. The slit scattering, which is responsible of the strong background, clearly imposes to introduce the propagation between the slit and the FZP (equal to 1.15m in our set-up) in our calculations. The best agreement of the far-field intensity is obtained for a slit opening of $72_v \times 28_h$ μm^2 (Fig. 4b). The discrepancy between these values and the expected ones of $60_v \times 20_h$ μm^2 is attributed to an error in the calibration of the slit. The case of an identically open slit located directly at the FZP is shown in Fig. 4c. In Fig. 4a, the non-zero intensity pixels in the center of the detector are due to direct beam photons transmitted by the central stop (most likely higher harmonics).

5. Reconstruction of the focused complex wavefield from experimental data

The analysis of the experimental data are performed using the phase retrieval approach described in section 2.3. To facilitate the algorithm convergence, the simulated phase at the detector plane was used as initial guess in the retrieval algorithm. The non-zero intensity pixels in the center of the detector (Fig. 4a) have been masked for the reconstruction. Results obtained from the inversion are shown in Fig. 5a. The range in x and y-directions is limited by the detector resolution. The wavefield at the focus of the FZP in the illumination conditions which better reproduce our data (cf. Fig. 4a), is shown in Fig. 5b. This calculation is used as comparison for the reconstructed wavefield. The size of the reconstructed focal spot is $\approx 280_v \times 730_h$ nm^2 (Fig. 5a) and the focal depth is equal to ≈ 1.76 mm (Fig. 6). The asymmetry of the focal spot in the horizontal direction compares very well with the calculations (cf. Fig. 5b). A similar asymmetry is found also in the vertical direction, which is not expected from the simulations. This effect is attributed to the peculiar illumination of the FZP obtained with vertical slit blades with an offset in the longitudinal direction [37]. Most interestingly, the reconstructed phase is constant in the focal spot (Fig. 5a).

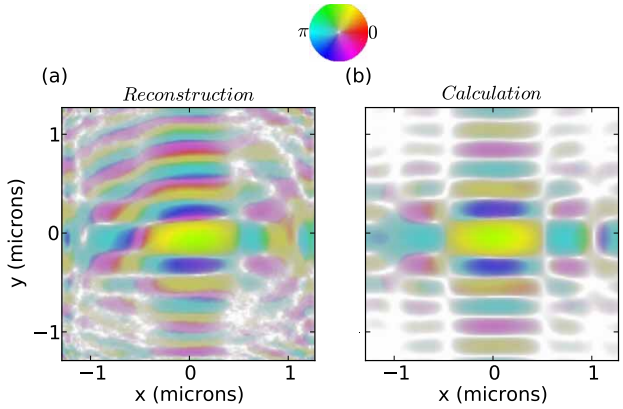

Fig. 5. (a) Color rendition of the reconstructed complex-valued field at the focal plane compared to (b) the calculated propagation of Fig. 4b back to the focal plane. The phase is represented by colors and the amplitude (in logarithmic scale) by colors intensities.

#146854 - $15.00 USD Received 5 May 2011; revised 3 Jun 2011; accepted 3 Jun 2011; published 19 Sep 2011

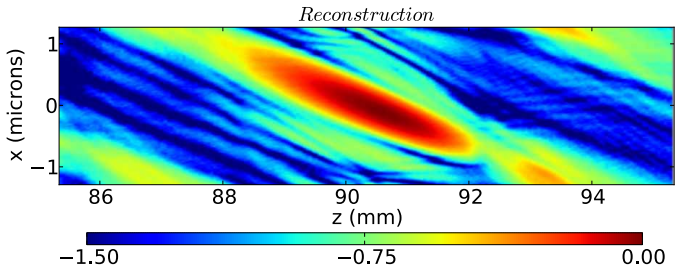

Fig. 6. Section of the reconstructed wavefield in the direction of propagation. The amplitude is expressed in logarithmic scale.

6. Conclusions

In this study we provide a numerical approach to characterize the coherent complex field at the focus of a partially illuminated circular FZP. Systematically varying the illumination conditions, we observe noteworthy changes in the characteristic sizes of the beam at the focal plane. Namely, the focal spot size and the focal depth are found to be diffraction limited, with size increasing by decreasing the illuminated area on the lens. By means of the proposed calculations, we demonstrate to be able to understand and predict the role of the different optical elements in our set-up, e.g. size and position of the slits defining the illumination of the FZP. In particular, we learned the importance of defining the partial illumination via an aperture placed very close to the FZP. This helps avoiding diffraction effects which could induce asymmetric intensity of the focal spot. This has an important impact for a reliable characterization of nanoscale objects using coherent diffraction techniques both in Bragg geometry, where the crystal deformation is encoded in the phase of the reconstructed complex function, and in forward direction. Finally, calculations of the far field amplitude produced by a partially illuminated FZP, have been used to support the reconstruction of the complex illumination function at the focal plane from experimental data. Even in presence of an asymmetry of the focal spot, due to the specific set-up used, the reconstructed wavefront has been found to have a constant phase within the central spot, in agreement with our calculations. The use of the new set-up recently developed at the beamline ID01 will provide us with new opportunities for a direct wavefront characterizations, through the increased resolution for the measurement of the far field data, and a better control of the illumination conditions of the focusing optics. The use of the ptychography approach on a test sample, for the characterization of the wavefield produced by FZP in the same illumination conditions presented in this manuscript is also planned. This is expected to give us a comparison with the presented results.

Acknowledgments

The authors are grateful to the ID01 beamline staff for the technical support during measurements at the ESRF. This work has been partially performed under the French ANR (ANR-08-JCJC-0095-01).

#146854 - $15.00 USD Received 5 May 2011; revised 3 Jun 2011; accepted 3 Jun 2011; published 19 Sep 2011